Photoelectron holographic study for atomic sites occupancy for Si dopant in Si-doped κ-Ga_2O_3(001)

Yuhua Tsai,[1,2] Yusuke Hashimoto,[3] ZeXu Sun,[3] Takuya Moriki,[3] Takashi Tadamura,[3] Takahiro Nagata,[1] Piero Mazzolini,[4,5] Antonella Parisini,[4] Matteo Bosi,[5] Luca Seravalli,[5] Tomohiro Matsushita,[3] and Yoshiyuki Yamashita[1,2,*]

[1]National Institute for Materials Science, Tsukuba, Ibaraki 305-0044, Japan

[2]Department of Applied Chemistry, Faculty of Engineering, Kyushu University, Fukuoka 819-0395, Japan

[3]Nara Institute of Science and Technology, Ikoma, Nara 630-0192, Japan

[4]Department of Mathematical Physical and Computer Sciences, University of Parma, Parco Area delle Scienze 7/A, 43124 Parma, Italy

[5]IMEM-CNR, Parco Area delle Scienze 37/A, 43124 Parma, Italy

*E-mail: YAMASHITA.Yoshiyuki@nims.go.jp

Abstract

We investigated atomic sites occupancy for the Si dopant in Si-doped κ-Ga_2O_3(001) using photoelectron spectroscopy (PES) and photoelectron holography (PEH). From PES and PEH, we found that the Si dopant had one chemical state and three types of inequivalent Si substitutional sites (Si_{Ga}) were formed. The ratios for the

inequivalent tetrahedral, pentahedral, and octahedral Si_{Ga} sites were estimated to be 55.0%, 28.1%, and 16.9%, respectively. Higher (lower) ratios for the three inequivalent Si_{Ga} sites may come from lower (higher) formation energy. The Tetra (Octa) Si_{Ga} site has the highest (lowest) ratio of the three Si_{Ga} sites since it has the lowest (highest) formation energy. We suggest that the tetrahedral Si_{Ga} site is due to the active dopant site, whereas the pentahedral and octahedral Si_{Ga} sites can be attributed to the inactive dopant sites for the Si-doped κ-Ga_2O_3(001).

KEYWORDS: Ga_2O_3, κ-Ga_2O_3, Si-doped κ-Ga_2O_3, photoelectron holography

In recent years, gallium oxide (Ga_2O_3) has attracted considerable interest as an ultra-wide bandgap semiconductor because of a bandgap of around 5 eV, high thermal stability, and the availability of large-scale β-Ga_2O_3 single crystal wafers. Such superior Ga_2O_3 properties can apply to the field of power electronics.[1-7] For Ga_2O_3, there are five crystal polymorphs: α-, β-, δ-, γ-, and κ-Ga_2O_3.[3,4] Among them, the most thermodynamically stable is β-Ga_2O_3, which has been widely investigated.[6-9]

Recently, the orthorhombic κ-Ga_2O_3 polymorph is gaining attention due to its higher symmetry with respect to monoclinic structure, its large spontaneous polarization along the (001) direction, and its ferroelectricity.[10-13] According to previous studies, this structure can be synthesized by several chemical- and physical-vapor phase epitaxial techniques (e.g., metal-organic vapor phase epitaxy MOVPE, halide vapor phase epitaxy, molecular beam epitaxy, and pulsed laser deposition) on various substrates.[14] Among them, c-plane sapphire has been so far the most frequently used substrate for κ-Ga_2O_3 epitaxy.[7,15-18] The κ-Ga_2O_3 structure is shown in Figure 1(a). There are three inequivalent Ga atomic sites in κ-Ga_2O_3: octahedral (Octa), pentahedral (Penta), and tetrahedral (Tetra).[11,19]

For κ-Ga_2O_3, both Si and Sn have been experimentally found to be extrinsic donors.[7,11,16,20,21] According to electron paramagnetic resonance (EPR), Si is suggested to

be an effective mass donor when it is positioned as a substitutional of Ga (Si_{Ga}) in the tetrahedral site of the orthorhombic κ-Ga_2O_3 lattice.[16] Nonetheless, despite the possible incorporation of Si at cation concentrations that might exceed 1% in the metal-organic vapor phase deposited (MOVPE) layers, the reported Hall-measured charge carrier density *n* never exceeded the mid 10^{18} cm^{-3} range.[7] This net donor density concentration range was independently confirmed by capacitance-voltage measurements performed in Schottky diodes based on Si-doped κ-Ga_2O_3.[22]

In this framework, the following could all play an important role in the resulting Si dopant activation efficiency in κ-Ga_2O_3:[7] (i) the presence of a large concentration of extended defects (*i.e.*, rotational domain boundaries and plane defects), (ii) the possible occupation of different reticular Ga sites, and (iii) the presence of a large amount of compensating defects (deep level acceptors). In particular for point (i) and (iii), the (001)-oriented heteroepitaxy of κ-Ga_2O_3 on various substrates [*e.g.*, c-plane sapphire, (0001)-GaN, (111)-MgO][14] results in the formation of large density of structural defects that are mostly perfectly vertically oriented, *i.e.*, 3 x 120° rotated domains and anti-phase boundaries.[7,23,24] According to the recent work of Vyvenko *et al.*, these vertically oriented structural defects could be electrically charged.[24] We believe that the discrepancy between the detected level of incorporated Si in the κ-Ga_2O_3 matrix and the net doping level is in

line with a high level of compensation that can be largely induced by such vertically oriented structural defects. A similar picture of large charge carrier compensation related to charged structural defects has been reported and modelled in the case of defective β-Ga_2O_3 layers by Fiedler *et al.*[25] In this work, we describe the first experimental confirmation that the Si impurities incorporated in κ-Ga_2O_3 lattice sites substitute Ga (target point (ii)), particularly to experimentally clarify the respective fraction of different reticular Ga sites that are actually occupied by Si (Si_{Ga}), possibly causing active and inactive dopant in Si-doped κ-Ga_2O_3 thin films.

We employed photoelectron holography (PEH) to clarify the Si dopant site for the Si-doped κ-Ga_2O_3. In the PEH, the photoelectrons of the target atoms (*e.g.*, dopants) are excited as the emitter under photoirradiation and scattered by the surrounding atoms. Finally, interference patterns are formed in the core-level photoelectron angular distribution. PEH has a great advantage in which non-periodic atomic structures are applicable. Additionally, since PEH is based on photoelectron spectroscopy, chemical state-discriminated PEHs can be achieved.[26-29] Therefore, we can clarify the atomic structures and the chemical states of the Si dopants in κ-Ga_2O_3. The PEH schematic is shown in Figure 1(b).

We also performed PEH simulations for the atomic position of the Si dopants in

κ-Ga_2O_3 to clarify the Si dopant sites. Since the structure around the dopant atom should be relaxed as the dopant is introduced into κ-Ga_2O_3, the bond length around the dopant atom may be different from the length before the dopant introduction. Thus, we performed extended x-ray absorption fine structure (EXAFS) to estimate the bond length after the dopant introduction. PEH simulations were done using the bond length after introducing the dopant. In the present study, we investigated the atomic position of the Si dopant for Si-doped κ-Ga_2O_3 using PEH to clarify the atomic structures of the active and inactive Si dopants for the Si-doped κ-Ga_2O_3.

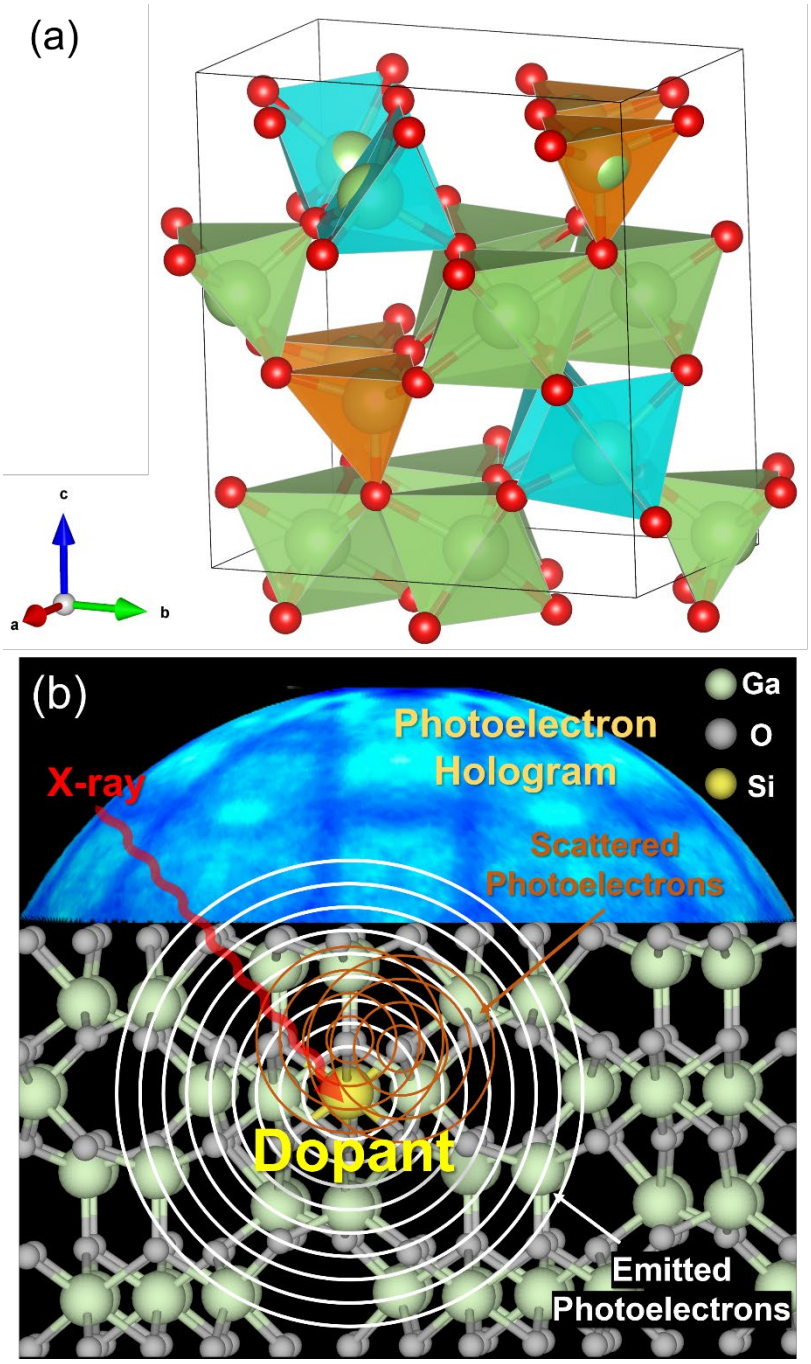

Figure 1. (a) Unit cell of κ-Ga_2O_3: Green, blue, and brown polyhedrons represent Octa, Penta, and Tetra Ga sites. (b) PEH schematic for Si-doped κ-Ga_2O_3. Yellow, green, and gray balls represent Si, Ga, and O atoms.

A κ-Ga_2O_3 epitaxial layer was grown on a c-plane sapphire substrate with

MOVPE. Trimethylgallium and ultrapure H_2O were used as a metal precursor and an oxidizing gas. H_2 was used as the gas carrier. The reaction was carried out at a H_2 pressure of 60 mbar in the growth chamber with a substrate temperature of 610°C. A H_2-diluted mixture of 0.05% SiH_4 was employed as the Si dopant source. Using a SiH_4 flow of 15 standard cubic centimeters per minute resulted in a Si concentration of 1.02 cation % in the κ-Ga_2O_3 layer (determined by atom probe tomography, which is the same sample that was previously investigated.) evenly distributed in the analyzed film volume.[7] The dopant's carrier concentration was experimentally determined by Hall effect measurements to be 2.6×10^{18} cm^{-3} where the electronic transport was dominated by a hopping mechanism (further details on the electrical characterization of the very same sample are available.).[7] Before PES and PEH measurements, the substrates were cleaned by the RCA method so that surface contaminations were removed. Then the surface oxide layer and the particles were removed by concentrated hydrochloric acid for 1 min., followed by washing with deionized water.

X-ray photoelectron spectroscopy (XPS) and hard x-ray photoelectron spectroscopy (HAXPES) measurements were performed using PHI Quantes (ULVAC-PHI). Monochromatic Al Kα (1486.6 eV) and Cr Kα (5414.9 eV) were used as incident x-rays sources for the XPS and HAXPES. The take-off angle (TOA) was 90° (surface

normal). We employed the pass energies of 55 and 112 eV for XPS and HAXPES measurements, respectively. The energy resolutions for XPS and HAXPES measurements were estimated to be 0.51 and 1.11 eV, respectively. The total energy resolutions were estimated by measuring the Fermi level of Au polycrystalline sample. We used KolXPD software to perform the XPS and HAXPES peaks fitting.[30] We used Voight function (convolution of Lorentzian and Gaussian functions) for peaks fitting after removal of the background of the Shirley function.[31-33]

PEH measurements were performed at BL25SU at SPring-8. We used a retarding field analyzer (RFA) for PEH measurements. The RFA energy resolution was approximately 0.5 eV.[34-36] RFA's acceptance angle was approximately ±49°, and the angular resolution was 0.5°.[36] The base pressure of the main chamber was 2.8×10^{-8} Pa. PEH simulations were performed using 3D-AIR-IMAGE software (version 1.1.09). The total analysis multiple scattering pattern simulation code was included in the software.[37-40] For the simulations, we employed an electron kinetic energy of 800 eV, a temperature of 300 K, and an inelastic mean free path of 10 Å.

The EXAFS measurements were carried out at the BL6N1 in the Aichi Synchrotron Radiation Center. The base pressure of the main chamber was 3.1×10^{-7} Pa. The spot-size of the incident photon at the sample position was 2.0 mm × 1.0 mm

(horizontal × vertical). A SPECS PHOIBOS 150 was used as an electron analyzer.[41] The pass energy was set to 20 eV. The angle between the incident photon and the sample surface normal was 55°. The TOA was set to 90° (surface normal).[42,43] For the EXAFS measurements, the total electron yield was employed. The energy range for the EXAFS measurements was from 1800 to 2100 eV with 1.0 eV energy steps.

Figure 2 shows the XPS and HAXPES spectra for the Si-doped κ-Ga_2O_3(001). In the Ga 2*p* XPS spectrum (Figure 2(a)), the peak at 1119.0 eV is attributed to the Ga-O species.[44-46] In the Si 1*s* HAXPES spectrum (Figure 2(b)), the peak at 1843.5 eV is due to the Si-O species.[47,48] When the different Si oxidation states (from 1^+ to 4^+) exist, the corresponding peaks appear at lower binding energy position from 1 to 3 eV (depend on the oxidation states),[49,50] forming an asymmetric peak structure. However, the Si 1*s* HAXPES spectrum shows a symmetric peak structure. Therefore, we can exclude the possibility of the presence of the different Si oxidation states. Thus, the chemical state of the Ga and Si atoms shows one chemical component. Since Si 1*s* shows one chemical

species, the Si atom in the Si-O species may be due to the Si dopants.

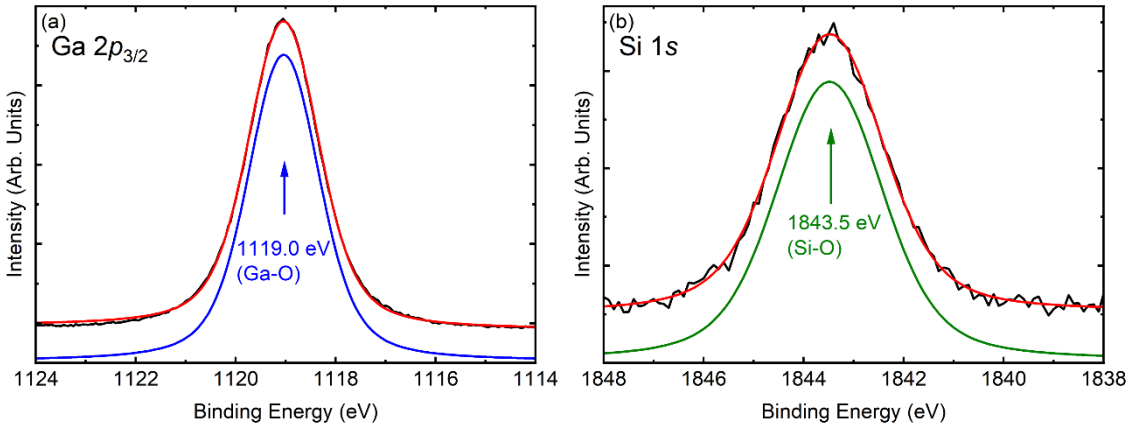

Figure 2. (a) Ga $2p_{3/2}$ XPS (b) Si 1*s* HAXPES spectra measured at photon energies of 1486.6 eV (XPS) and 5414.9 eV (HAXPES), respectively.

Figure 3(a) shows the Ga 3*p* and Si 2*p* PES spectrum for the Si-doped κ-Ga_2O_3(001) measured at an incident photon energy of 911 eV. For them, spin-orbit splitting of 3.46 eV and 0.60 eV was employed for the peaks fitting.[51-54] The corresponding PEHs for Ga 3*p* and Si 2*p* are shown in Figures. 3(b) and (c). The Si 2*p* PEH shows clear patterns, indicating that the Si dopant may be located at the atomic positions of κ-Ga_2O_3(001).

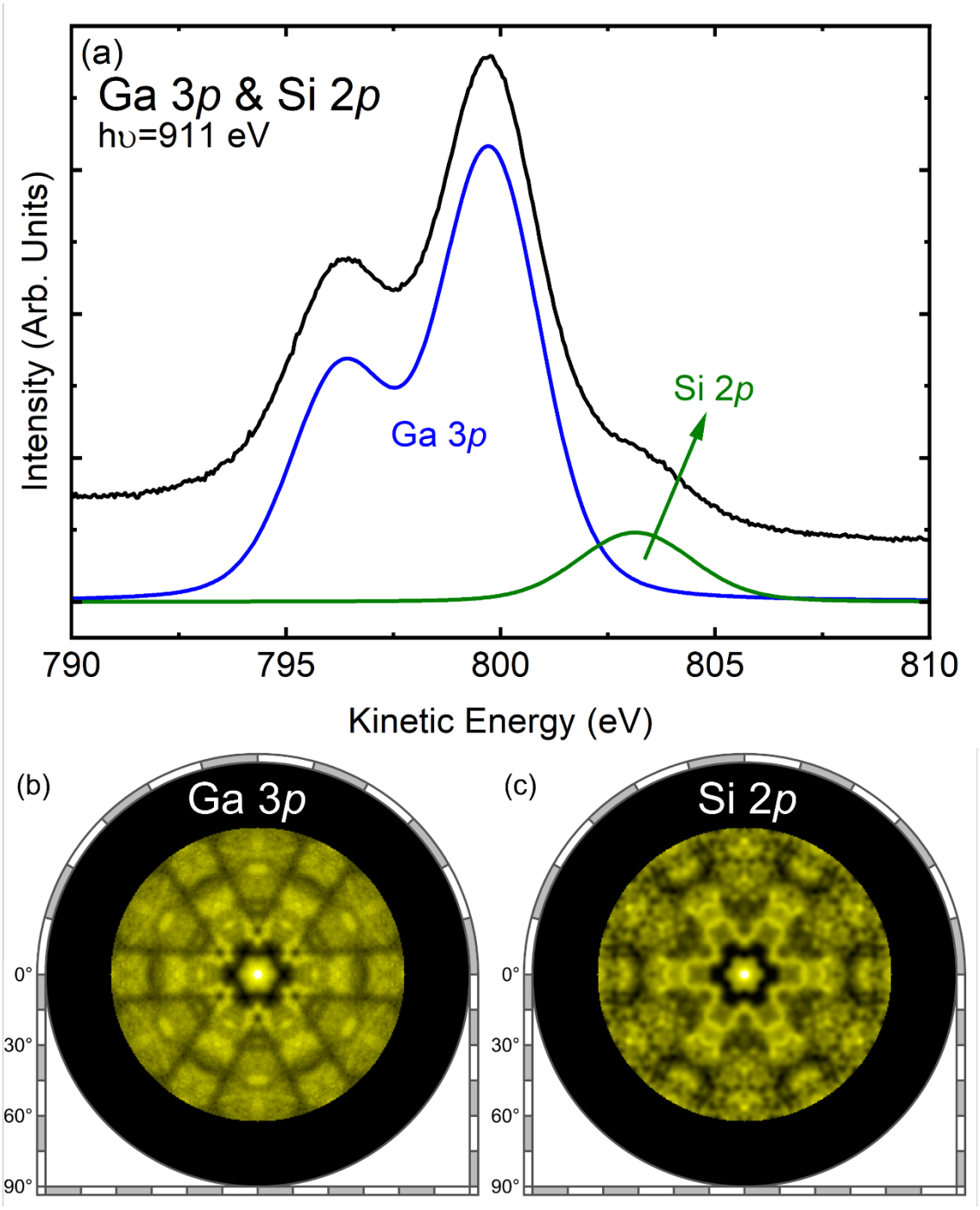

Figure 3. (a) Ga 3*p* and Si 2*p* PES spectrum for Si-doped κ-Ga_2O_3(001). PEHs of (b) Ga 3*p* and (c) Si 2*p* for Si-doped κ-Ga_2O_3(001).

Figures 4(a) and (b) show the EXAFS and the oscillation for the Si-doped κ-Ga_2O_3(001). Fig. 4(c) shows k^2-weighted Si *K*-edge EXAFS spectrum plotted with the

fitting result for Si-doped κ-Ga_2O_3(001). The fitting range in k-space was chosen at 2–7.2 $Å^{-1}$ with a good signal-to-noise ratio. Fig. 4(d) shows the radial distribution function of the k^2-weighted EXAFS and the fitting result of the Octa Si_{Ga} site as an example. The fitting was performed using ARTEMIS software, and the reliable factor was set to 0.015.[55,56] The nearest Si-O distance was estimated to be 2.01 Å, a value shorter than the Ga-O bond length of 2.02 Å observed for the non-doped κ-Ga_2O_3 Octa site.[23]

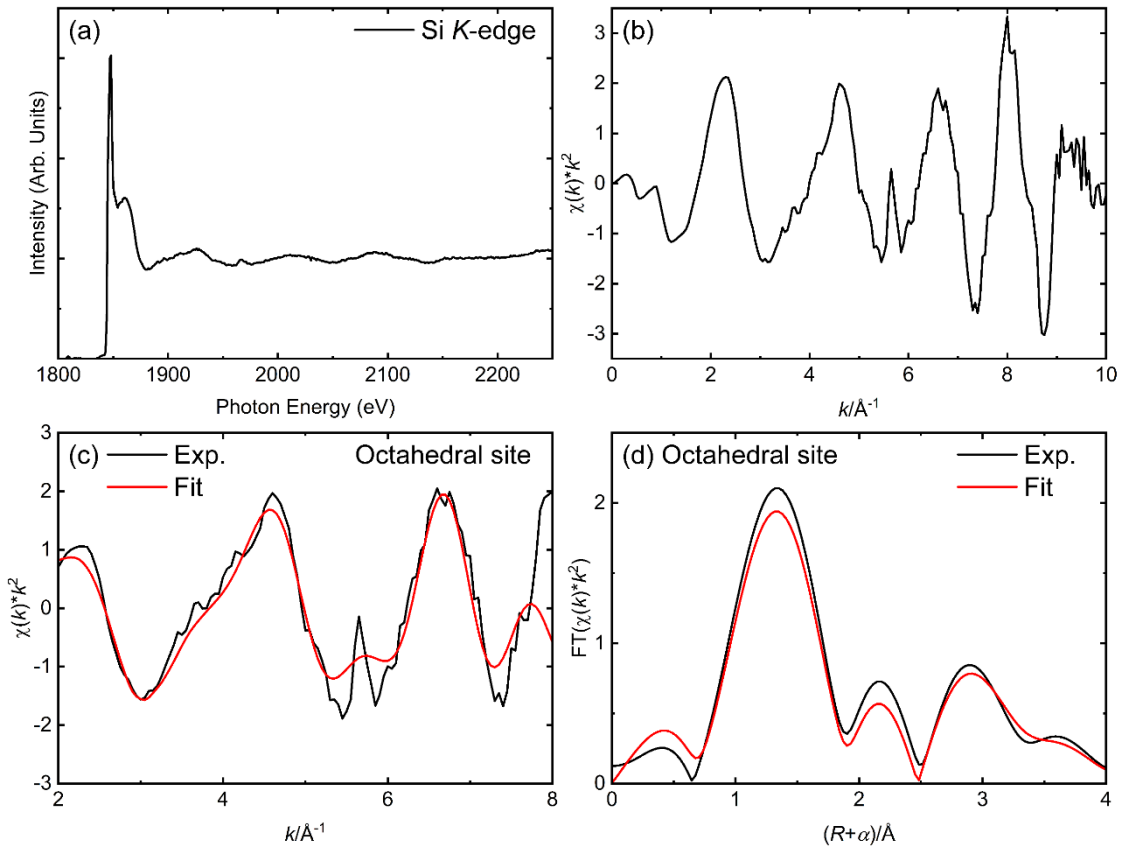

Figure 4. (a) Si *K*-edge EXAFS and (b) k^2-weighted Si *K*-edge EXAFS for Si-doped κ-Ga_2O_3(001). (c) k^2-weighted Si *K*-edge EXAFS spectrum (black solid line) plotted with best fit (red solid line) for Si-doped κ-Ga_2O_3(001) sample. The fitting range was 2–7.2 $Å^{-1}$. (d) Radial distribution function of the k^2-weighted EXAFS (black solid line) and the fitting results (red solid line) for Si_{Ga} in Octa site. The fitting range was 1–4 Å. The amplitude reduction factors, ΔR, and MSRD values were set to 1, -0.011 Å, and 0.015, respectively.

We also performed fitting for the other Si_{Ga} sites in κ-Ga_2O_3 (Figure S2). The first nearest Si-O distance was estimated to be 2.02 Å and 1.83 Å for the Penta and Tetra Si_{Ga} sites. We performed PEH simulations based on the bond length obtained from EXAFS. This is because when the dopants are introduced to the sample, the bond length should be changed around the dopant atom. Thus, we have to use the bond lengths around the Si dopant atom obtained from EXAFS.

According to previous studies, dopant atomic positions are Ga replaced by Si, that is, Si_{Ga} in κ-Ga_2O_3.[7,20] Therefore, PEH simulations were performed for the Octa, Penta, and Tetra Si_{Ga} sites. Figure 5 shows the experimental and simulated Si 2*p* PEHs for the Octa, Penta, and Tetra Si_{Ga} sites. Not every simulated PEH for the respective Octa, Penta, and Tetra Si_{Ga} sites explains the experimental Si 2*p* PEH, indicating that the Si dopant sites may be due to the mixture of inequivalent Si_{Ga} sites.

To determine the dopant site ratio for the Si-doped κ-Ga_2O_3, we mixed the simulated Si 2*p* PEHs of the Tetra, Penta, and Octa Si_{Ga} sites. The simulated PEH with the three inequivalent Si_{Ga} site ratios is shown in Figure 5(d). The best fit for the experimental PEH data was obtained using the ratios for Tetra, Penta, and Octa Si_{Ga} sites of 55.0%, 28.1%, and 16.9%, respectively. Note that the occupancy ratios of the Tetra, Penta, and Octa Si_{Ga} sites were estimated using the equations shown in Supporting Information.

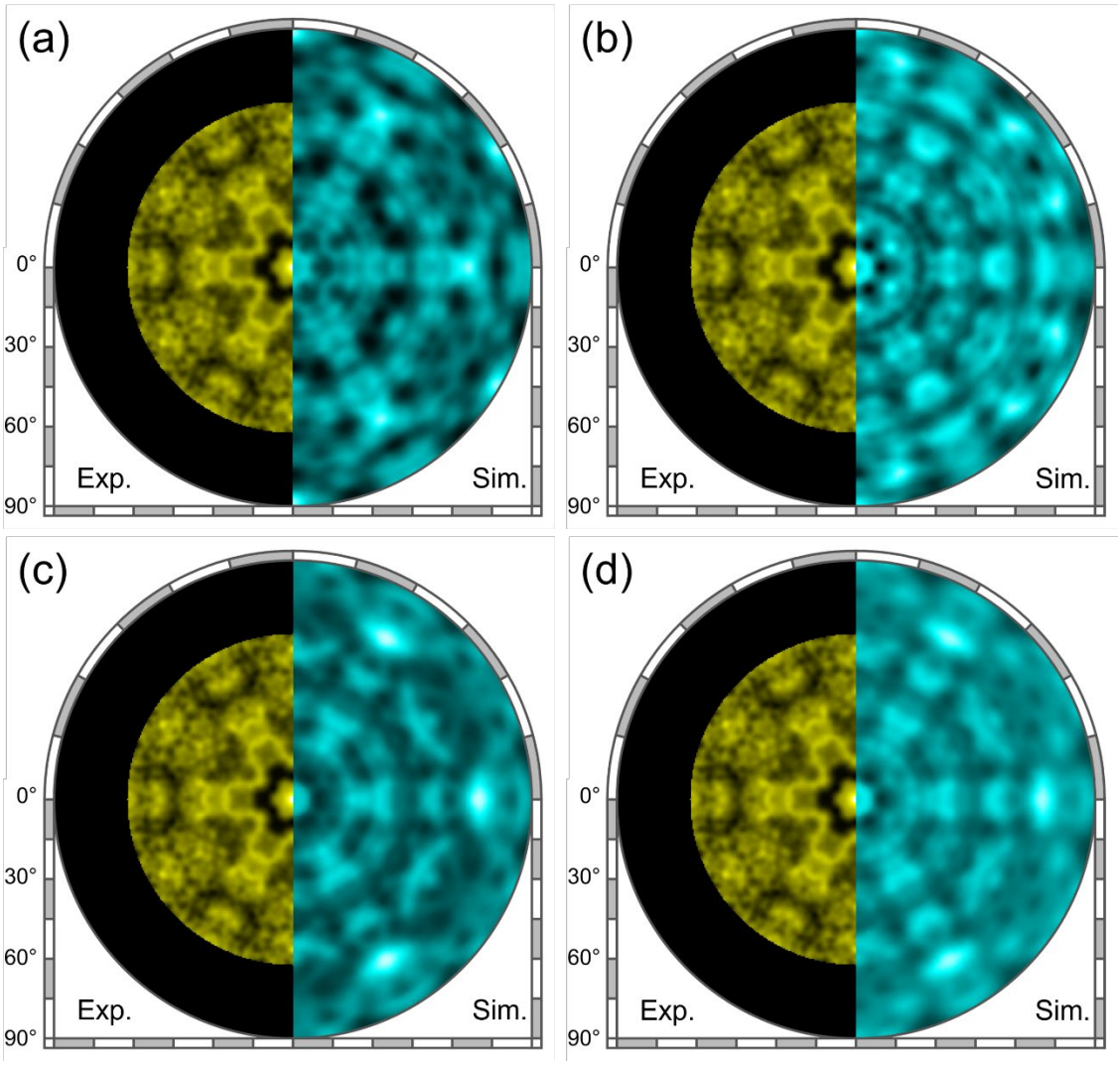

Figure 5. Experimental (yellow) Si 2*p* and the simulated (blue) PEHs. The simulated PEHs of (a) Octa Si_{Ga} site (b) Penta Si_{Ga} site (c) Tetra Si_{Ga} site, and (d) their sum are 16.9%, 28.1%, and 55.0%.

For the undoped κ-Ga_2O_3, the ratios for the Tetra, Penta, and Octa sites were 25%, 25%, and 50%.[11,19] Therefore, based on our results, in the case of the Si-doped κ-Ga_2O_3, the Tetra Si_{Ga} site is strongly favored with respect to the Penta and Octa sites (55.0% with respect to the presence of just 25% of the Ga tetrahedral sites in the κ-Ga_2O_3 lattice). The Penta Si_{Ga} (28.1%) is almost half of the tetrahedral site occupation despite sharing an identical amount of available sites in the orthorhombic lattice (25% of the

Penta Ga sites in the undoped κ-Ga_2O_3). Even though the Octa Ga sites are the highest occupation in the κ-Ga_2O_3 lattice (50%), the Octa Si_{Ga} site occupation in Si-doped κ-Ga_2O_3 is the lowest (16.9%).

The difference in these Si_{Ga} ratios might be related to the formation energy of such defects. In this framework, our data suggest that the Tetra sites of the Si_{Ga} defect should have the lowest formation energy with respect to the Octa and Penta coordinations. Nevertheless, this does not fully agree with the first principles calculations of Zeman et al. that predicted the Octa Si_{Ga} site to have the lowest formation energy for the κ polymorph, followed by the Tetra and Penta sites.[57]

The discrepancy between the experimental and theoretical results might be explained as follows. As we already described the introduction section, our sample has large density of structural defects. The defects are mostly perfectly vertically oriented, *i.e.*, 3 x 120° rotated domains and anti-phase boundaries.[7,23,24] In addition, these vertically oriented structural defects could be electrically charged.[24] On the other hand, the first principles calculations of Zeman et al. do not contain the charged structural defects, vertically oriented and rotated domains, and anti-phase boundaries.[57] As a result, the first principles calculations might not fully agree with the experimental results.[58-60]

Von Bardeleben et al. investigated the electrically active dopant in Si-doped κ-

Ga_2O_3 with EPR and concluded that the detected dopant site was due to the Tetra Si_{Ga} site.[16] Thus, based on the present investigation, that site may be attributed to the active dopant site for the Si-doped κ-Ga_2O_3. The Si impurity in other Ga sites might be electrically inactive dopants for the Si-doped κ-Ga_2O_3 (Penta and Octa Si_{Ga} sites). Further investigations are required to clarify the origin of the suggested inactivity of the Si_{Ga} Penta and Octa sites.

We used XPS, HAXPES, PEH, and EXAFS to clarify the chemical states and the atomic positions of Si dopants for Si-doped κ-Ga_2O_3(001). From XPS and HAXPES, we found that the Si dopant shows one chemical state for the Si-O species in Si-doped κ-Ga_2O_3(001). Since the Si 2*p* PEH showed clear hologram patterns for the Si dopant, it should be located at the cationic positions of κ-Ga_2O_3(001). We experimentally demonstrated that Si is effectively incorporated in Ga sites. We simulated the PEH patterns to clarify the precise occupation site of Si dopants in the orthorhombic lattice and found that the simulated PEH of each inequivalent Si_{Ga} site (i.e., Tetra, Penta, Octa) could not explain the experimental Si 2*p* PEH. Thus, the Si dopant was found to occupy all the different cationic sites (i.e., mixture of inequivalent Si_{Ga} sites). With the ratios of the Tetra, Penta, and Octa Si_{Ga} sites of 55.0%, 28.1% and 16.9%, respectively, we obtained a best fit of the PEH experimental data. The recorded differences should be considered in light

of the overall amount of different Ga inequivalent sites in the orthorhombic unit cell (i.e., Tetra, Penta, and Octa sites of 25%, 25%, and 50%) and may be attributed to different Si_{Ga} formation energies. In this framework, the Tetra Si_{Ga} site has by far the highest occupation ratio among the three inequivalent Ga sites in the lattice. We suggest that this result is related to the Si_{Ga} in the Tetra site that has the lowest formation energy; whereas, the Octa Si_{Ga} site exhibited the lowest ratio, suggesting that this defect configuration has the highest formation energy. The current findings in the framework of previous investigations suggest that the Tetra Si_{Ga} site may be the only active dopant site in Si-doped κ-Ga_2O_3, and the Penta and Octa Si_{Ga} sites may be inactive.

Supporting Information

The supporting information contains additional experimental data. Figure S1 shows Si 2*s* XPS spectrum of Si-doped κ-Ga_2O_3(001). Figure S2 shows k^2-weighted Si *K*-edge EXAFS and the radial distribution function of the k^2-weighted EXAFS and the fitting results for the Penta and the Tetra Si_{Ga} sites for Si-doped κ-Ga_2O_3(001) sample. Figure S3 shows the difference images between experimental PEH and simulated PEHs for Octa, Penta, Tetra Si_{Ga} sites, and the sum of Octa, Penta, and Tetra Si_{Ga} sites where the respective ratio of 16.9%, 28.1%, and 55.0% (the best fit). (Figure 5(d))

Acknowledgments

We acknowledge Dr. H. Oji at the Aichi Synchrotron Center for the experimental support. The synchrotron radiation experiments were performed with the approval of the Japan Synchrotron Radiation Research Institute (JASRI, proposal no. 2023A1221). This work was supported by JSPS Grant-in-Aid for Transformative Research Areas (A) "Hyper-Ordered Structures Science": Grant Number 20H05882, 20H05884. This work was also supported by JSPS KAKENHI: Grant Number 20H01841. The epitaxial growth of Ga_2O_3 is supported by Italian National Recovery and Resilience Plan (PNRR) funded by NextGenerationEU, Mission 4, Component 2, Project "Ecosystem for Sustainable Transition in Emilia-Romagna - (Ecosister)".

Author Contributions

Y.Y. designed, planned, led the research. Data analysis was performed by Y.T and Y.Y. P.M., A.P., M.B. and L.S. fabricated the Si-doped κ-Ga_2O_3 samples. Y.T., Z.S., T.M., T.T. and T.N. performed the experiments under the supervision of Y.H., T.M. and Y.Y.

References

(1) Pearton, S. J.; Yang, J.; Cary, P. H.; Ren, F.; Kim, J.; Tadjer, M. J.; Mastro, M. A. A Review of Ga_2O_3 materials, processing, and devices. *Appl. Phys. Rev.* **2018**, *5*, 011301.

(2) Zhang, J.; Shi, J.; Qi, D.-C.; Chen, L.; Zhang, K. H. Recent progress on the electronic structure, defect, and doping properties of Ga_2O_3. *APL Mater.* **2020**, *8*, 020906.

(3) Kaneko, K.; Uno, K.; Jinno, R.; Fujita, S. Prospects for phase engineering of semi-stable Ga_2O_3 semiconductor thin films using mist chemical vapor deposition. *J. Appl. Phys.* **2022**, *131*, 090902.

(4) Wang, Y.; Su, J.; Lin, Z.; Zhang, J.; Chang, J.; Hao, Y. Recent progress on the effects of impurities and defects on the properties of Ga_2O_3. *J. Mater Chem. C* **2022**, *10*, 13395–13436.

(5) Hu, Z.; Feng, Q.; Feng, Z.; Cai, Y.; Shen, Y.; Yan, G.; Lu, X.; Zhang, C.; Zhou, H.; Zhang, J.; Hao, Y. Experimental and Theoretical Studies of Mo/Au Schottky Contact on Mechanically Exfoliated β-GA_2O_3 Thin Film. *Nanoscale Res. Lett.* **2019**, *14*, 1–7.

(6) Jamwal, N. S.; Kiani, A. Gallium Oxide Nanostructures: A Review of Synthesis, Properties and Applications. *Nanomaterials* **2022**, *12*, 2061.

(7) Mazzolini, P.; Fogarassy, Z.; Parisini, A.; Mezzadri, F.; Diercks, D.; Bosi, M.; Seravalli, L.; Sacchi, A.; Spaggiari, G.; Bersani, D.; Bierwagen, O.; Janzen, B.; Marggraf, M.; Wagner, M.; Cora, I.; Pécz, B.; Tahraoui, A.; Bosio, A.; Borelli, C.; Leone, S.; Fornari, R. Silane-Mediated Expansion of Domains in Si-Doped κ-Ga_2O_3 Epitaxy and its Impact on the In-Plane Electronic Conduction. *Adv. Funct. Mater.* **2022**, *33*, 2207821.

(8) Tippins, H. H. Optical Absorption and Photoconductivity in the Band Edge of β-Ga_2O_3. *Phys. Rev.* **1965**, *140*, A316.

(9) Mu, S.; Van de Walle, C. G. Phase stability of $(Al_xGa_{1-x})_2O_3$ polymorphs: A first-principles study. *Phys. Rev. Mater.* **2022**, *6*, 104601.

(10) Mezzadri, F.; Calestani, G.; Boschi, F.; Delmonte, D.; Bosi, M.; Fornari, R. Crystal Structure and Ferroelectric Properties of ε-Ga_2O_3 Films Grown on (0001)-Sapphire. *Inorg. Chem.* **2016**, *55*, 12079–12084.

(11) Kang, H. Y.; Choi, Y.; Pyeon, K.; Lee, T. H.; Chung, R. B. Experimental and theoretical investigation of the effect of Sn on κ-Ga_2O_3 Growth. *J. Mater. Sci.* **2022**, *57*, 19882–19891.

(12) Cho, S. B.; Mishra, R. Epitaxial engineering of polar ε-Ga_2O_3 for tunable two-dimensional electron gas at the heterointerface. *Appl. Phys. Lett.* **2018**, *112*, 162101.

(13) Ranga, P.; Cho, S. B.; Mishra, R.; Krishnamoorthy, S. Highly tunable, polarization-engineered two-dimensional electron gas in ε-$AlGaO_3$/ε-Ga_2O_3 heterostructures. *Appl. Phys. Express* **2020**, *13*, 061009.

(14) Bosi, M.; Mazzolini, P.; Seravalli, L.; Fornari, R. Ga_2O_3 polymorphs: tailoring the epitaxial growth conditions. *J. Mater. Chem. C* **2020**, *8*, 10975–10992.

(15) Janzen, B. M.; Mazzolini, P.; Gillen, R.; Peltason, V. F.; Grote, L. P.; Maultzsch, J.; Fornari, R.; Bierwagen, O.; Wagner, M. R. Comprehensive Raman study of orthorhombic κ/ε-Ga2O3 and the impact of rotational domains. J. Mater Chem. C 2021, 9, 14175–14189.

(16) von Bardeleben, H. J.; Cantin, J. L.; Parisini, A.; Bosio, A.; Fornari, R. Conduction mechanism and shallow donor properties in silicon-doped ε-Ga_2O_3 thin films: An electron paramagnetic resonance study. *Phys. Rev. Mater.* **2019**, *3*, 084601.

(17) Girolami, M.; Bosi, M.; Serpente, V.; Mastellone, M.; Seravalli, L.; Pettinato, S.; Salvatori, S.; Trucchi, D. M.; Fornari, R. Orthorhombic undoped κ-Ga_2O_3 epitaxial thin films for sensitive, fast, and stable direct X-ray detectors. *J. Mater Chem. C* **2023**, *11*, 3759–3769.

(18) Ardenghi, A.; Bierwagen, O.; Lähnemann, J.; Kler, J.; Falkenstein, A.; Martin, M.; Mazzolini, P. Phase-selective growth of κ- vs β-Ga_2O_3 and $(In_xGa_{1-x})_2O_3$ by In-mediated metal exchange catalysis in plasma-assisted molecular beam epitaxy. arXiv (physics.app-ph). 2023-11-22. https://doi.org/10.48550/arXiv.2311.13318. (accessed 2024-03-01).

(19) Seacat, S.; Lyons, J. L.; Peelaers, H. Properties of orthorhombic Ga_2O_3 Alloyed with In_2O_3 and Al_2O_3. *Appl. Phys. Lett.* **2021**, *119*, 042104.

(20) Parisini, A.; Bosio, A.; Montedoro, V.; Gorreri, A.; Lamperti, A.; Bosi, M.; Garulli, G.; Vantaggio, S.; Fornari, R. Si and Sn doping of ε-Ga_2O_3 Layers. *APL Mater.* **2019**, *7*, 031114.

(21) Polyakov, A.; Lee, I.; Nikolaev, V.; Pechnikov, A.; Miakonkikh, A.; Scheglov, M.; Yakimov, E.; Chikiryaka, A.; Vasilev, A.; Kochkova, A.; Shchemerov, I.; Chernykh, A.; Pearton, S. Properties of κ-Ga_2O_3 Prepared by Epitaxial Lateral Overgrowth. *Adv. Mater. Interfaces* **2023**, 2300394.

(22) Rajabi Kalvani, P.; Parisini, A.; Sozzi, G.; Borelli, C.; Mazzolini, P.; Bierwagen, O.; Vantaggio, S.; Egbo, K.; Bosi, M.; Seravalli, L.; Fornari, R. Interfacial Properties of the SnO/κ-Ga_2O_3 p-n Heterojunction: A Case of Subsurface Doping Density Reduction via Thermal Treatment in κ-Ga_2O_3. *ACS Appl. Mater. Interfaces 2023, 15, 45997−46009*.

(23) Cora, I.; Mezzadri, F.; Boschi, F.; Bosi, M.; Čaplovičová, M.; Calestani, G.; Dódony, I.; Pécz, B.; Fornari, R. The real structure of ε-Ga_2O_3 and its relation to κ-phase. *Cryst. Eng. Comm.* **2017**, *19*, 1509–1516.

(24) Vyvenko, O. F.; Shapenkov, S. V.; Ubyivovk, E. V.; Bondarenko, A. S.; Pechnikov, A. I.; Nikolaev, V. I.; Stepanov, S. I. Twin domain and antiphase boundaries in microcrystals of K-Phase Ga_2O_3. *Materialia* **2023**, *32*, 101942.

(25) Fiedler, A.; Schewski, R.; Baldini, M.; Galazka, Z.; Wagner, G.; Albrecht, M.; Irmscher, K. Influence of incoherent twin boundaries on the electrical properties of β-Ga_2O_3 layers homoepitaxially grown by metal-organic vapor phase epitaxy. *J. Appl. Phys.* **2017**, *122* (16), 165701.

(26) Tsutsui, K.; Matsushita, T.; Natori, K.; Muro, T.; Morikawa, Y.; Hoshii, T.; Kakushima, K.; Wakabayashi, H.; Hayashi, K.; Matsui, F.; Kinoshita, T. Individual Atomic Imaging of Multiple

Dopant Sites in As-Doped Si Using Spectro-Photoelectron Holography. *Nano Lett.* **2017**, *17*, 7533–7538.

(27) Tang, J.; Takeuchi, S.; Tanaka, M.; Tomita, H.; Hashimoto, Y.; Nagata, T.; Chen, J.; Ohkochi, T.; Kotani, Y.; Matsushita, T.; Yamashita, Y. Direct Observation of Atomic Structures and Chemical States of Active and Inactive Dopant Sites in Mg-Doped GaN. *ACS Appl. Electron. Mater.* **2022**, *4*, 4719–4723.

(28) Yokoya, T.; Terashima, K.; Takeda, A.; Fukura, T.; Fujiwara, H.; Muro, T.; Kinoshita, T.; Kato, H.; Yamasaki, S.; Oguchi, T.; Wakita, T.; Muraoka, Y.; Matsushita, T. Asymmetric Phosphorus Incorporation in Homoepitaxial P-Doped (111) Diamond Revealed by Photoelectron Holography. *Nano Lett.* **2019**, *19*, 5915–5919.

(29) Uenuma, M.; Kuwaharada, S.; Tomita, H.; Tanaka, M.; Sun, Z.; Hashimoto, Y.; Fujii, M. N.; Matsushita, T.; Uraoka, Y. Atomic structure analysis of gallium Oxide at the Al_2O_3/GaN interface using photoelectron holography. *Appl. Phys. Express* **2022**, *15*, 085501.

(30) Libra, J. *KolXPD: Software for Spectroscopy Data Measurement and Processing*, version 1.8.0 (build 68); Kolibrik.net: Czech, 2021. (accessed 2024-03-01).

(31) Jain, V.; Biesinger, M. C.; Linford, M. R. The Gaussian-Lorentzian Sum, Product, and Convolution (Voigt) functions in the context of Peak Fitting X-ray photoelectron spectroscopy (XPS) narrow scans. *Appl. Surf. Sci.* **2018**, *447*, 548–553.

(32) Castle, J. E.; Salvi, A. M. Interpretation of the Shirley background in x-ray photoelectron spectroscopy analysis. *J. Vac. Sci. Technol. A* **2001**, *19*, 1170–1175.

(33) Végh, J. The Shirley Background Revised. *J. Electron Spectros. Relat. Phenomena* **2006**, *151*, 159–164.

(34) Muro, T.; Ohkochi, T.; Kato, Y.; Izumi, Y.; Fukami, S.; Fujiwara, H.; Matsushita, T. Wide-angle display-type retarding field analyzer with high energy and angular resolutions. *Rev. Sci. Instrum.* **2017**, *88*, 123106.

(35) Muro, T.; Matsushita, T.; Sawamura, K.; Mizuno, J. Spherical micro-hole grid for high-resolution retarding field analyzer. *J. Synchrotron. Radiat.* **2021**, *28*, 1669–1671.

(36) Matsushita, T.; Hashimoto, Y.; Tomita, H.; Sun, Z.; Kawamura, S.; Fujii, M. N.; Mizuno, J. An Algorithm to Correct the Sensitivity Distribution of a Retarding Field Analyzer for Photoelectron Holography. *e-J. Surf. Sci. Nanotechnol.* **2023**, *21*, 183–187.

(37) Matsushita, T.; Matsui, F.; Daimon, H.; Hayashi, K. Photoelectron holography with improved image reconstruction. *J. Electron. Spectrosc.* **2010**, *178*, 195–220.

(38) Matsushita, T. Algorithm for Atomic Resolution Holography Using Modified L_1-regularized Linear Regression and Steepest Descent Method. *Phys. Status. Solidi. B* **2018**, *255*, 180091.

(39) Li, Y.; Sun, Z.; Kataoka, N.; Setoguchi, T.; Hashimoto, Y.; Takeuchi, S.; Koga, S.; Demura, S.; Noguchi, K.; Sakata, H.; Mizuguchi, Y.; Matsushita, T.; Wakita, T.; Muraoka, Y.; Yokoya, T.

Photoelectron Holography Study of La(O,F)BiS_2. *J. Phys. Soc. Jpn.* **2023**, *92*, 044801.

(40) Matsushita, T.; Muro, T.; Yokoya, T.; Terashima, K.; Kato, Y.; Matsui, H.; Maejima, N.; Hashimoto, Y.; Matsui, F. Theory for High-angular-resolution Photoelectron Holograms Considering the Inelastic Mean Free Path and the Formation Mechanism of Quasi-Kikuchi Band. *Phys. Status. Solidi. B* **2020**, *257*, 2000117.

(41) Oji, H.; Murai, T.; Shibata, Y.; Tabuchi, M.; Watanabe, Y.; Takeda, Y. Current Status of BL6N1 of AichiSR: A Tender X-Ray Beamline for XAFS and Photoemission Spectroscopy. *J. Surf. Anal.* **2020**, *26*, 228–244.

(42) Indari, E. D.; Yamashita, Y.; Hasunuma, R.; Oji, H.; Yamabe, K. Relationship between electrical properties and interface structures of SiO_2/4H-SiC prepared by dry and wet oxidation. *AIP Adv.* **2019**, *9*, 105018.

(43) Yamashita, Y.; Nara, J.; Indari, E. D.; Yamasaki, T.; Ohno, T.; Hasunuma, R. Experimental and theoretical studies on atomic structures of the interface states at SiO_2/4H-SiC(0001) interface. *J. Appl. Phys.* **2022**, *131*, 215303.

(44) Bhuiyan, A. F.; Feng, Z.; Huang, H.-L.; Meng, L.; Hwang, J.; Zhao, H. MOCVD growth and band offsets of κ-phase Ga_2O_3 on c-plane sapphire, GaN- and AlN-on-sapphire, and (100) YSZ substrates. *J. Vac. Sci. Technol. A* **2022**, *40*, 062704.

(45) Hellwig, M.; Xu, K.; Barreca, D.; Gasparotto, A.; Winter, M.; Tondello, E.; Fischer, R. A.; Devi, A. Novel Gallium Complexes with Malonic Diester Anions as Molecular Precursors for the MOCVD of Ga_2O_3 Thin Films. *Eur. J. Inorg. Chem.* **2009**, *2009*, 1110–1117.

(46) Ghosh, S. C.; Biesinger, M. C.; LaPierre, R. R.; Kruse, P. X-ray photoelectron spectroscopic study of the formation of catalytic gold nanoparticles on ultraviolet-ozone oxidized GaAs(100) substrates. *J. Appl. Phys.* **2007**, *101*, 114322.

(47) Vanleenhove, A.; Hoflijk, I.; Vaesen, I.; Zborowski, C.; Artyushkova, K.; Conard, T. High-energy x-ray photoelectron spectroscopy spectra of SiO_2 measured by Cr Kα. *Surf. Sci. Spectra* **2022**, *29*, 014014.

(48) Chourasia, A. R.; Hood, S. J.; Chopra, D. R. A study of Si compounds by Zr *L*α photoelectron spectroscopy. *J. Vac. Sci. Technol. A* **1996**, *14*, 699–703.

(49) Kobayashi, K. High-resolution hard X-ray photoelectron spectroscopy: Application of valence band and core-level spectroscopy to materials science. *Nucl. Instrum. Meth. A* **2005**, *547*, 98–112.

(50) Zhang, L.; Kuramoto, N.; Azuma, Y.; Kurokawa, A.; Fujii, K. Thickness Measurement of Oxide and Carbonaceous Layers on a ^{28}Si Sphere by XPS. *IEEE T. Instrum. Meas.* **2016**, *66*, 1297–1303.

(51) Gibbon, J. T.; Jones, L.; Roberts, J. W.; Althobaiti, M.; Chalker, P. R.; Mitrovic, I. Z.; Dhanak, V. R. Band alignments at Ga_2O_3 heterojunction interfaces with Si and Ge. *AIP Adv.* **2018**, *8*, 065011.

(52) Thompson, A.; Attwood, D.; Gullikson, E.; Howells, M.; Kim, K. J.; Kirz, J.; Winick, H. X-ray

data booklet; Lawrence Berkeley National Laboratory, Uiversity of California: Berkeley, CA, 2001

(53) Ulgut, B.; Suzer, S. XPS Studies of SiO_2/Si System under External Bias. *J. Phys. Chem. B* **2003**, *107*, 2939–2943.

(54) Nesbitt, H. W.; Bancroft, G. M.; Davidson, R.; Mcintyre, N. S.; Pratt, A. R. Minimum XPS core-level line widths of insulators, including silicate minerals. *Am. Mineral.* **2004**, *89*, 878–882.

(55) Ravel, B.; Newville, M. *ATHENA*, *ARTEMIS*, *HEPHAESTUS*: data analysis for X-ray absorption spectroscopy using *IFEFFIT*. *J. Synchrotron Radiat.* **2005**, *12*, 537–541.

(56) Ravel, B.; Newville, M. ATHENA and ARTEMIS: interactive graphical data analysis using IFEFFIT. *Phys. Scripta* **2005**, *2005*, 1007.

(57) Zeman, C. J.; Kielar, S. M.; Jones, L. O.; Mosquera, M. A.; Schatz, G. C. Investigation of p-type doping in β- and κ-Ga_2O_3. *J. Alloy. Compd.* **2021**, *877*, 160227.

(58) Shokri, A.; Melikhov, Y.; Syryanyy, Y.; Demchenko, I. N. Point Defects in Silicon-Doped β-Ga_2O_3: Hybrid-DFT Calculations. *ACS Omega* **2023**, *8*, 43732–43738.

(59) Tadjer, M. J.; Lyons, J. L.; Nepal, N.; Freitas, J. A.; Koehler, A. D.; Foster, G. M. Review-Theory and Characterization of Doping and Defects in β-Ga_2O_3. *ECS J. Solid State SC.* **2019**, *8*, Q3187–Q3194.

(60) Lany, S. Defect phase diagram for doping of Ga_2O_3. *APL Mater.* **2018**, *6*, 046103.